



Contents lists available at [ScienceDirect](#)

Journal of Science: Advanced Materials and Devices

journal homepage: www.elsevier.com/locate/jsamd



Original Article

Spin-phonon interaction in nanocrystalline $Dy_3Fe_5O_{12}$ probed by Raman spectroscopy: Effects of magnetic ordering



Bojan Stojadinović ^{a,*}, Zorana Dohčević-Mitrović ^{a,**}, Sonja Aškrabić ^a, Novica Paunović ^a, M.T. Rahul ^b, B. Raneesh ^b, Nandakumar Kalarikkal ^{c,d}

^a Institute of Physics Belgrade, University of Belgrade, Pregrevica 118, 11080, Belgrade, Serbia

^b Department of Physics, Catholicate College, Pathanamthitta, Kerala, 689 645, India

^c School of Pure and Applied Physics, Mahatma Gandhi University, Kottayam, 686 560, India

^d International & Inter University Centre for Nanoscience and Nanotechnology, Mahatma Gandhi University, Kottayam, Kerala, 686 560, India

ARTICLE INFO

Article history:

Received 2 February 2023

Received in revised form

24 May 2023

Accepted 27 June 2023

Available online 7 July 2023

Keywords:

Rare-earth iron garnets
 $Dy_3Fe_5O_{12}$ nanoparticles
Raman spectroscopy
Spin-phonon interaction

ABSTRACT

We report the effects of magnetic ordering on the temperature evolution of the Raman modes in nanocrystalline $Dy_3Fe_5O_{12}$. The $Dy_3Fe_5O_{12}$ was synthesized by an aqueous sol–gel method. X-ray diffraction, Raman spectroscopy and transmission electron microscopy studies revealed the phase purity and nanocrystalline nature. We particularly focused on the spin-phonon coupling mechanism in $Dy_3Fe_5O_{12}$, as this interaction can greatly affect the magnetoelectric and multiferroic properties of $Dy_3Fe_5O_{12}$. Below T_C , four phonon modes from the middle- and high-frequency regions displayed anomalous behavior, which was ascribed to the spin-phonon interaction. The application of the mean-field approach enabled us to quantify the spin-phonon coupling strength for each of these phonon modes. Our study has shown that different phonon modes are coupled to ferromagnetic or antiferromagnetic ordering depending on the type of vibrational motion characteristic for a specific mode. These results significantly enhance the understanding of the complex spin-phonon coupling mechanism and its implications on the multifaceted properties of nanocrystalline $Dy_3Fe_5O_{12}$, such as multiferroic, magnetoelectric, and magnetocaloric properties. Moreover, these findings have the potential to drive advancements in the optimization and development of spintronic devices.

© 2023 Vietnam National University, Hanoi. Published by Elsevier B.V. This is an open access article under the CC BY-NC-ND license (<http://creativecommons.org/licenses/by-nc-nd/4.0/>).

1. Introduction

Ferrimagnetic rare earth (RE) iron garnets, with general formula $RE_3Fe_5O_{12}$, present an important class of magnetic insulators due to their interesting magnetic properties, such as the formation of canted magnetic (double umbrella-like) structure and the huge magnetostriction at low temperatures [1]. Interesting magneto-optical properties [2–4], low magnetic losses in the microwave region, and the appearance of a magnetocaloric effect [5] made them attractive materials for magneto-optic devices, microwave circuits, or magnetic refrigeration applications. The discovery of the magneto-electric and magnetodielectric effects in RE iron garnets

renewed the interest in these materials [6]. In recent years, the possibility of tailoring magnetic properties by changing the material morphology and reducing the grain size to nanometric dimensions focused the research interest towards the nanocrystalline forms of RE iron garnets. These materials, with peculiar magnetic properties, are expected to be particularly useful for the low-temperature refrigeration and spintronic applications [5,7,8].

Among the RE iron garnets, dysprosium iron garnet ($Dy_3Fe_5O_{12}$) exhibits numerous attractive physical properties, such as huge magnetostriction [1] and magnetic and magneto-optical properties [9,10]. The observed anisotropic magnetodielectric, magnetocaloric, and magnetoelectric effects [11–14] imply that $Dy_3Fe_5O_{12}$ may be a promising material for the applications in various novel magnetodielectric, magnetocaloric, and spintronic functional devices in future [15].

In RE iron garnets, due to the complexity of magnetic interactions, the coupling between the spin and lattice vibrations can greatly influence their magnetic, magnetocaloric or

* Corresponding author.

** Corresponding author.

E-mail addresses: bojans@ipb.ac.rs (B. Stojadinović), zordoh@ipb.ac.rs (Z. Dohčević-Mitrović).

Peer review under responsibility of Vietnam National University, Hanoi.

magnetoelectric properties. The spin-phonon interaction plays an important role in the spin relaxation processes, or the spin reorientation transition, and can affect the ultrafast magnetic phenomena [16]. Yet, the interplay between spins and phonons in RE iron garnets is almost unstudied. Furthermore, the study of the spin-phonon coupling mechanism in multiferroic nanostructures is of great importance because the spins and phonons can be strongly coupled with the lattice strain, influencing at the same time the ferroelectric ordering and the coupling between electric polarization and the magnetization ordering [17]. It is worth to mention that the microscopic origin of the recently discovered large magnetoelectric effect and multiferroic phase in $Dy_3Fe_5O_{12}$ is still unclear [11]. Therefore, a better understanding of the spin-phonon coupling mechanism in nanocrystalline $Dy_3Fe_5O_{12}$ is very important both from the fundamental and application point of view. Raman scattering spectroscopy is a highly sensitive and effective method for studying spin dynamics and the effects of exchange coupling between magnetic ions and phonons. This technique also allows to estimate the strength of the spin-phonon coupling in ferromagnetic (FM), ferrimagnetic, or antiferromagnetic (AFM) materials by analyzing the temperature evolution of the Raman mode frequencies at and below the magnetic transition temperature.

To our knowledge, the spin-phonon interaction in RE iron garnets, except for the yttrium iron garnet [18], was not studied before. The lack of such studies and knowing that $Dy_3Fe_5O_{12}$ has a more complex magnetic structure than yttrium iron garnet motivated us to investigate the effects of magnetic ordering on optical phonon modes in nanocrystalline $Dy_3Fe_5O_{12}$ analyzing the temperature-dependent Raman spectra. Within the mean-field approach, we were able to quantify the spin-phonon coupling strength of the phonon modes, which were sensitive to magnetic ordering. These results advance the understanding of the spin-phonon interaction in nanocrystalline $Dy_3Fe_5O_{12}$ and can play an important role in better understanding of multiferroic, magnetoelectric or magnetocaloric properties of RE iron garnets.

2. Experimental

The nanocrystalline $Dy_3Fe_5O_{12}$ was prepared by an aqueous sol-gel method. Iron nitrate ($Fe(NO_3)_3 \cdot 9H_2O$) and dysprosium oxide (Dy_2O_3) were used as starting materials. Firstly, a stoichiometric amount of dysprosium oxide was dissolved in nitric acid. In the following step, 100 ml of deionized water and a stoichiometric amount of $Fe(NO_3)_3 \cdot 9H_2O$ were added to the solution. The chelating agent PVA was added to the solution (the molar ratio of the total metal ions to the PVA = 1:1), and the solution was stirred for several hours at 55–65 °C. The formed gel was dried in an oven (120 °C) for 24 h. Finally, the dry gel was calcined at 800 °C for 3 h in the air.

The crystalline structure of nanocrystalline $Dy_3Fe_5O_{12}$ was analysed using a Rigaku MiniFlex X-ray diffractometer in the 2θ range of 15–80°, with the step width of 0.01° and the scanning rate of 5°/min. Transmission electron microscopy (TEM) image of the sample was collected using a JEOL JEM 2100 transmission electron microscope. Energy dispersive X-ray analysis (EDAX) was conducted using an Oxford EDAX system attached to a JEOL JEM 2100 transmission electron microscope. Temperature-dependent micro-Raman spectra of nanocrystalline $Dy_3Fe_5O_{12}$ (pressed into pellets) were collected in a backscattering configuration using a TriVista 557 triple spectrometer, with the spectral resolution of 2 cm^{-1} . The temperature measurements from 80 to 700 K were performed in a Linkam THMSG600 cooling/heating stage. The argon/krypton ion laser with an emitting line at $\lambda = 514.5\text{ nm}$ was used as an excitation source, with the output laser power kept at less than 2 mW to avoid

the heating effects and/or sample degradation. The Raman spectra were corrected by the Bose-Einstein thermal occupation factor. The magnetization vs. temperature was measured in the 6–315 K temperature range in a magnetic field of 10 kOe, using a vibrating sample magnetometer in a high field measuring system (HFMS, Cryogenic Ltd).

3. Results and discussion

$Dy_3Fe_5O_{12}$ crystallizes in a cubic crystal structure with space group O_h^{10} ($Ia3d$). The conventional unit cell consists of eight formula units $Dy_3Fe_2(FeO_4)_3$. Fe^{3+} ions occupy 16a octahedral (Fe^0) and 24d tetrahedral (Fe^T) sites, and Dy^{3+} ions occupy 24c dodecahedral sites. These three cation sites are surrounded by O^{2-} oxygen ions (see inset of Fig. 1(a)). The X-ray diffraction (XRD) pattern of nanocrystalline $Dy_3Fe_5O_{12}$ sample is illustrated in Fig. 1(a).

The XRD peaks are indexed to the body-centered cubic $Dy_3Fe_5O_{12}$ crystalline structure with the O_h^{10} ($Ia3d$) space group (JCPDS 23–0237). No impurity phases were detected. The average crystallite size, calculated by Scherrer formula, was 60 nm. Fig. 1(b) shows the TEM image of nanocrystalline $Dy_3Fe_5O_{12}$ sample. The particles of different sizes (approximately 30–80 nm) and irregular shapes can be observed in the TEM image. The captured HRTEM image of the sample (Fig. 1(c)) exhibits clear lattice planes, and the distance between the adjacent planes is ~0.28 nm. The measured plane distance matches with the (420) reflection of the $Dy_3Fe_5O_{12}$ crystal. The Selected Area Electron Diffraction (SAED) pattern, presented in the inset of Fig. 1(c), shows a large number of bright spots confirming the polycrystalline structure of the prepared $Dy_3Fe_5O_{12}$ sample. The EDAX spectrum of $Dy_3Fe_5O_{12}$, given in Fig. 1(d), shows the signature peaks of Dy, Fe and O elements. Moreover, the peaks from Cu were also noticed, which originate from the Cu grid used for dispersing the $Dy_3Fe_5O_{12}$ particles for the imaging and EDAX studies. The weight and atomic percentage of constituent elements (with and without Cu content) are listed in Table 1. From EDAX analysis it can be concluded that the stoichiometry of $Dy_3Fe_5O_{12}$ sample is very close to the anticipated values.

Factor group analysis for the body-centered cubic garnet crystalline structure with O_h^{10} ($Ia3d$) space group predicts 25 Raman active modes (3 A_{1g} , 8 E_g and 14 T_{2g}) [19,20]. In Fig. 2(a) are presented Raman spectra of nanocrystalline $Dy_3Fe_5O_{12}$ in the 80–700 K temperature range. In order to follow the evolution of the Raman modes with temperature and to determine more precisely the mode frequency, the spectra from Fig. 2(a) were deconvoluted using Lorentzian-type profiles. The deconvoluted Raman spectra, for some selected temperatures, are presented in Fig. 2(b). The insets display the enlarged view of the high-frequency modes together with the best Lorentzian fits.

In Table 1 are presented the frequencies of the Raman modes, obtained from the deconvoluted Raman spectrum at 80 K (Fig. 2(b)). The modes are classified according to the symmetry assignments taken from the literature for iron garnets [21–23] and are compared with the data of Song et al. for $Dy_3Fe_5O_{12}$ crystal [21]. As can be seen, in the spectrum of nanocrystalline $Dy_3Fe_5O_{12}$ the number of the Raman modes is smaller than in the spectrum of $Dy_3Fe_5O_{12}$ crystal [21]. The appearance of fewer modes than predicted is a consequence of lower crystallinity of nanomaterials compared to the bulk counterparts.

The assignation of the Raman modes in iron garnets is very complex due to the presence of three different lattices in the garnet structure. Based on the lattice dynamical calculations of the Raman spectra in RE aluminum garnets [19, 20, 24], the high-frequency modes ($> 500\text{ cm}^{-1}$) can be assigned to the internal vibrations of the tetrahedral (FeO_4) units. In the middle-frequency region

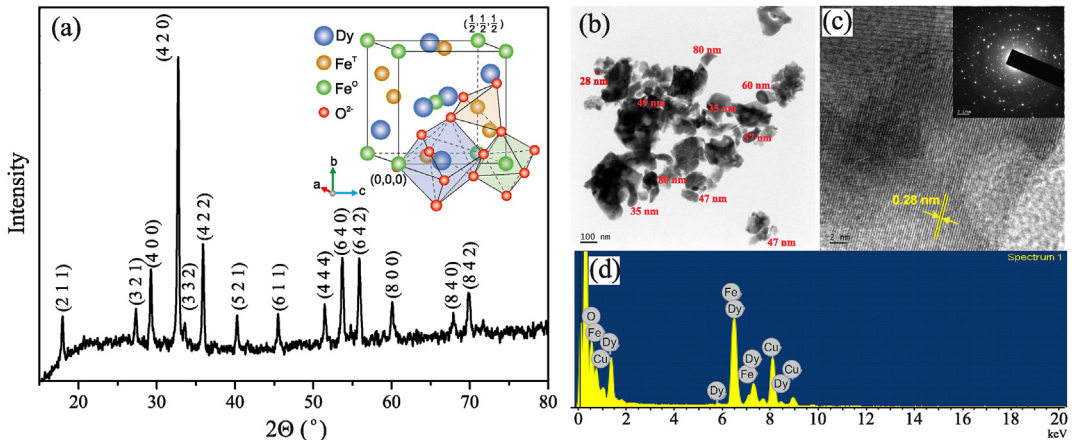


Fig. 1. (a) XRD pattern of the nanocrystalline $\text{Dy}_3\text{Fe}_5\text{O}_{12}$. The inset presents a garnet-type structure of space group O_h^{10} ($Ia3d$) with three distinct cation crystallographic sublattices surrounded by oxygen. (b) TEM image, (c) HRTEM image (SAED pattern is presented in the inset), and (d) EDAX spectrum of the nanocrystalline $\text{Dy}_3\text{Fe}_5\text{O}_{12}$.

Table 1

Estimated stoichiometry for $\text{Dy}_3\text{Fe}_5\text{O}_{12}$ sample from EDAX analysis. The left half of the table is with, and the right one is without Cu content.

Element	Weight % ±3%	Atomic % ±3%	Element	Weight % ±3%	Atomic % ±3%
O K	17.64	53.77	O K	21.38	62.84
Fe K	21.64	18.90	Fe K	26.08	21.96
Cu K	19.50	14.97	Dy L	52.54	15.20
Dy L	41.21	12.37	Total	100	100
Total	100	100			

(300–500 cm^{-1}), the E_g Raman modes correspond to the internal vibrations of the RE ions, tetrahedral Fe^{T} ions, and oxygen, where the RE and Fe^{T} ions can move in phase or in antiphase. T_{2g} modes from the middle-frequency region present a combination of internal and rotational modes of tetrahedral units. It can be concluded that the Raman modes from the middle-frequency region are more complex and of mixed character. The low-frequency modes ($< 300 \text{ cm}^{-1}$) were attributed to RE^{3+} , FeO_4 and/or FeO_6 translational modes [24,25]. At this point, it is worth mentioning the conclusions of Hurrell et al. [19], who pointed out that there is no apparent grouping of modes reflecting strong tetrahedral or octa-

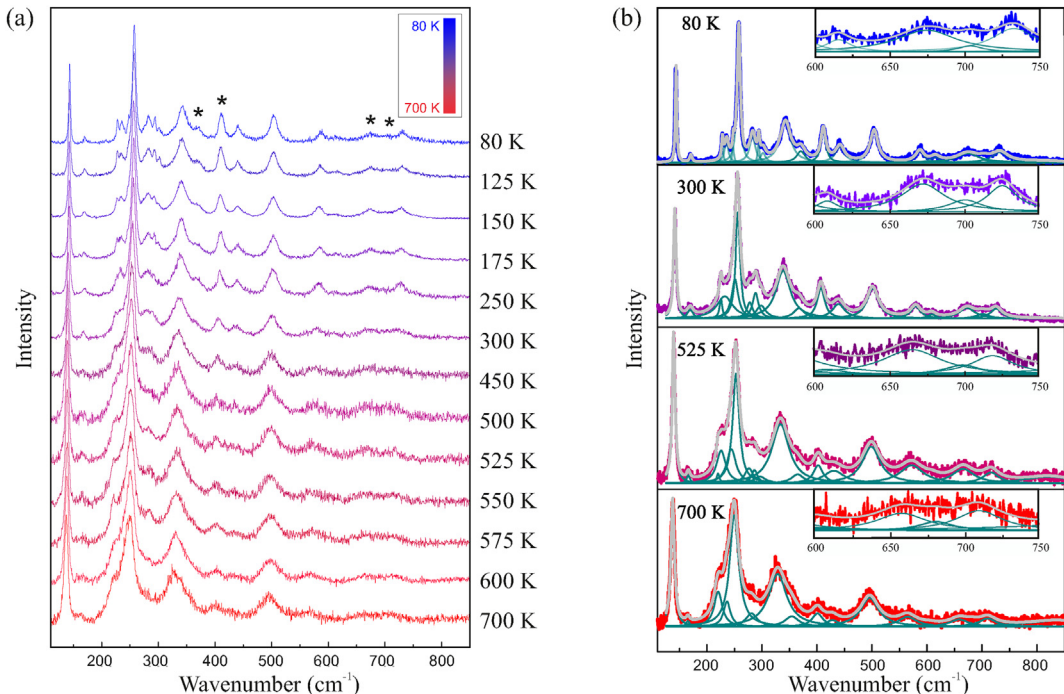


Fig. 2. Raman spectra of nanocrystalline $\text{Dy}_3\text{Fe}_5\text{O}_{12}$ (a) in the 80–700 K temperature range, and (b) at selected temperatures. The dark cyan lines represent Lorentzian fits of the experimental data and the grey lines are the cumulative fits. The anomalous phonon modes are marked with asterisk. The insets display the enlarged view of the high-frequency modes, together with individual and cumulative Lorentzian fits.

hedral bonding of the oxygen anions, as each oxygen atom belongs to one tetrahedron, one octahedron and two dodecahedra. Hurrell et al. also concluded that the Raman modes which do not involve the motion of cations (like A_{1g} modes), reflect more the octahedral vibrations of oxygen anions.

In magnetic materials, the exchange coupling between magnetic ions can affect phonon frequencies at and below the magnetic ordering temperature (T_C or T_N). In FM materials, for $T < T_C$, the temperature dependence of the phonon mode frequency ($\omega(T)$) can substantially deviate from the $\omega(T)$ behavior predicted by the phonon–phonon anharmonic model [26]:

$$\omega_{\text{anh}}(T) = \omega_{\text{anh}}(0) - A \left(1 + \frac{2}{e^{\frac{\hbar\omega(T)}{2k_B T}} - 1} \right), \quad (1)$$

where $\omega_{\text{anh}}(0)$ is the phonon frequency at 0 K, A is the anharmonic constant related to the three-phonon scattering strength, \hbar is Planck's constant and k_B is Boltzmann's constant.

In the paramagnetic phase, at temperatures above T_C , spin–phonon coupling effects diminish and become negligible compared to the anharmonic effects [27]. Therefore, purely anharmonic contribution to the phonon frequency can be extracted from the $\omega(T)$ dependence in the paramagnetic phase. In magnetically ordered state below T_C , an anomalous behavior of the phonon frequency is ascribed to the spin-lattice interaction [27–39]. As a result, the change of phonon frequency below T_C can be expressed as the sum of anharmonic ($\omega_{\text{anh}}(T)$) and spin-phonon ($\Delta\omega_{\text{s-ph}}(T)$) contributions: $\omega(T) = \omega_{\text{anh}}(T) + \Delta\omega_{\text{s-ph}}(T)$.

Based on the Heisenberg model for the nearest-neighbor spin interaction, the phonon frequency shift, due to the spin-phonon interaction [40], can be expressed as

$$\Delta\omega_{\text{s-ph}}(T) = \lambda \langle \mathbf{S}_i \cdot \mathbf{S}_j \rangle, \quad (2)$$

where λ is the spin-phonon coupling constant and $\langle \mathbf{S}_i \cdot \mathbf{S}_j \rangle$ is the spin–spin correlation function between the nearest-neighbor spins localized at the i th and j th site.

In magnetic materials with coexisting FM and AFM ordering, the $\Delta\omega_{\text{s-ph}}$ term, according to the theoretical model [41], can be expressed in the form:

$$\Delta\omega_{\text{s-ph}}(T) \propto -J \langle \mathbf{S}_i \cdot \mathbf{S}_j \rangle + K \langle \mathbf{S}_i \cdot \mathbf{S}_k \rangle, \quad (3)$$

where \mathbf{S}_i , \mathbf{S}_j and \mathbf{S}_k indicate the spin of the i th, j th and k th magnetic ion, and $\langle \mathbf{S}_i \cdot \mathbf{S}_j \rangle$ and $\langle \mathbf{S}_i \cdot \mathbf{S}_k \rangle$ are the spin correlation functions for the nearest-neighbor or the next nearest-neighbor interactions, respectively. The constants J and K are the spin dependent force constants of the lattice vibrations, and present the summation of second derivatives of the exchange integrals with respect to the phonon displacement. The constants J and K are associated with the FM and AFM nearest-neighbor or next nearest-neighbor exchange.

Assuming that the spin correlation functions $\langle \mathbf{S}_i \cdot \mathbf{S}_j \rangle$ and $\langle \mathbf{S}_i \cdot \mathbf{S}_k \rangle$ have the same temperature dependence, and that J and K have constant values for the same Raman mode [33,41], the above expression can be written in a simplified form:

$$\Delta\omega_{\text{s-ph}}(T) \propto (K - J) \langle \mathbf{S}_i \cdot \mathbf{S}_j \rangle. \quad (4)$$

Depending on the relative strength between the FM and AFM exchange interactions, from Eq. (4) follows that the frequency shift of the Raman mode will be positive or negative depending on the sign of the $(K - J)$ difference. Comparing Eq. (2) and Eq. (4) it is obvious that λ can take negative or positive values depending on whether the FM or AFM interaction is more dominant for the particular mode.

Knowing that in ferrimagnetic materials like iron garnets, the phonon frequencies can be influenced by magnetic ordering below T_C , and that anharmonic processes should dominate in paramagnetic phase at $T > T_C$, the $\omega(T)$ dependence for each Raman mode from Fig. 2(a) was fitted using three-phonon anharmonic model (Eq. (1)) for $T > T_C$. This analysis showed that four Raman modes from the middle- and high-frequency regions exhibited anomalous frequency behavior below T_C . The positions of these modes at 80 K are 370, 411, 674 and 703 cm⁻¹, respectively (see Table 2). The rest of the Raman modes have similar $\omega(T)$ dependence in the whole temperature range, which can be well fitted using Eq. (1). The $\omega(T)$ dependences for 370, 411, 674 and 703 cm⁻¹ modes, together with the anharmonic fits, are presented in Fig. 3, where the regions of paramagnetic and ferrimagnetic phases are clearly marked. The anomalous frequency softening of 370, 674 and 703 cm⁻¹ modes (Fig. 3(a), (c) and (d)), and hardening of the 411 cm⁻¹ mode (Fig. 3(b)), below T_C , imply that these modes are strongly affected by magnetic ordering.

$\text{Dy}_3\text{Fe}_5\text{O}_{12}$ is a ferrimagnetic material with three magnetic sublattices (see inset of Fig. 4, where M_d , M_a and M_c are the sublattice magnetizations). Fe^{3+} ions, located in tetrahedral d sites and octahedral a sites, are strongly coupled via AFM superexchange interaction ($\text{Fe}^{T(3+)} - \text{O}^{2-} - \text{Fe}^{O(3+)}$). Because of the unequal number of Fe ions in two magnetic sublattices, the magnetizations M_d and M_a are of different magnitudes, resulting in a ferrimagnetic ordering below T_C . The noncompensated resultant magnetization ($M_d - M_a$) is coupled antiparallelly to the magnetization of Dy ions (M_c) at dodecahedral c sites. The magnetization of $\text{Dy}_3\text{Fe}_5\text{O}_{12}$ is very dependent on temperature [13,42–45]. At very low temperatures, the magnetization of the Dy sublattice surpasses the resultant magnetization of Fe sublattices. With increasing temperature, the magnetization of the Dy sublattice falls off more quickly than that of the Fe sublattices, and at the compensation temperature, T_{comp} , the magnetizations of Dy and Fe sublattices are mutually compensated [1,13,43–45]. Above the T_{comp} , and up to the magnetic transition temperature $T_C = 525$ K, the resultant magnetization of the Fe sublattices predominates. In Fig. 4 is shown the measured magnetization vs. temperature for nanocrystalline $\text{Dy}_3\text{Fe}_5\text{O}_{12}$. The compensation temperature (T_{comp}) is around 225 K, in accordance with literature data [13,43–45].

Table 2

The frequencies (in cm⁻¹) and symmetry assignments of Raman active phonons in nanocrystalline $\text{Dy}_3\text{Fe}_5\text{O}_{12}$ at 80 K, compared with the data from Ref. [21].

Mode	Present work ±3 cm ⁻¹	Song et al. [21] ±3 cm ⁻¹
T_{2g}		101
T_{2g}	143	144
T_{2g}	170	173
T_{2g}	235	236
E_g	257	259
T_{2g}		276
E_g	283	285
T_{2g}		325
$E_g + A_{1g}$	342	347
T_{2g}	370	371
E_g	411	410
E_g		435
T_{2g}	442	448
T_{2g}	504	501
A_{1g}		507
T_{2g}	587	589
E_g		624
$E_g + T_{2g}$	674	676
$A_{1g} + T_{2g}$	703	695
$A_{1g} + T_{2g}$	732	734

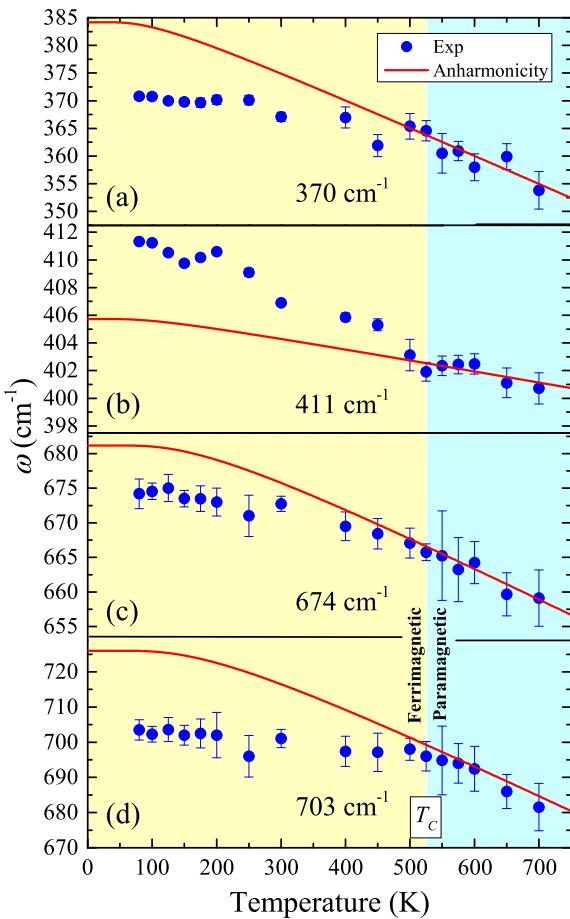


Fig. 3. Temperature dependence of the phonon frequencies (blue circles) at (a) 370, (b) 411, (c) 674, and (d) 703 cm⁻¹. The theoretically predicted anharmonic trend is presented by solid lines.

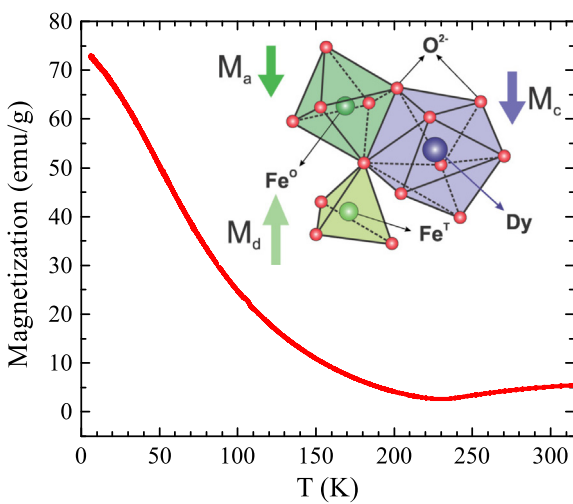


Fig. 4. Magnetization vs. temperature for nanocrystalline Dy₃Fe₅O₁₂. In the inset is given a schematic representation of three different magnetic sublattices of Dy₃Fe₅O₁₂ with polyhedra of oxygens.

In dysprosium iron garnet, among six different FM or AFM exchange interactions between the Fe and the Dy spins (three Fe–Fe interactions, two Fe–Dy interactions and one Dy–Dy interaction), the dominant superexchange interaction is between Fe spins in tetrahedral and octahedral sites (Fe^T–Fe^O interaction). The second

strongest interaction is AFM interaction between Dy and Fe^T spins (the first-nearest-neighbor Dy–Fe^T interaction) [44,46,47].

In materials with competitive FM and AFM interactions, like Dy₃Fe₅O₁₂, the exchange interactions between magnetic ions depend on their positions and on the positions of some nearby non-magnetic neighbors. On the other hand, each Raman mode involves vibrations of different magnetic and/or non-magnetic ions. Therefore, the contribution of FM or AFM exchange integrals to the spin dependent force constants (J and K in Eq. (3)) can be different for different modes [33,40,41]. As a result, the frequency shift due to the spin-phonon coupling (see Eq. (4)) will be negative or positive, depending on whether the FM or AFM exchange interaction is more dominant for a particular mode.

In magnetically ordered phase, the opposite frequency shifts of 370, 674 and 703 cm⁻¹ modes on one side, and the 411 cm⁻¹ mode on the other side, can be explained in the following way. The Raman modes at 674 and 703 cm⁻¹ are assigned to the internal vibrational modes of the tetrahedral (FeO₄) units, whereas the mode at 370 cm⁻¹ corresponds to a combination of rotational modes of the same units [20,23,24]. The ferromagnetic Fe^T – O – Fe^T exchange interactions between nearest-neighbor tetrahedral Fe^T ions can strongly affect the force constants of tetrahedral (Fe^T – O) vibrations. As a consequence, detectable changes in the phonon frequencies on entering the magnetic phase should be seen. According to the Eq. (4), the anomalous frequency softening of 370, 674 and 703 cm⁻¹ modes (Fig. 3(a), (c) and (d)) below T_C imply that these modes are effectively modulated by FM exchange interactions between Fe^T ions in the magnetically ordered phase. On the other hand, in RE iron garnets, some phonon modes from the middle-frequency region can be sensitive to the AFM ordering between the RE and Fe^T ions. The Raman mode at 411 cm⁻¹ involves the motion of dodechaedral Dy ions, tetrahedral Fe³⁺ ions and oxygen ions [24]. Hence, it is reasonable to assume that the antiferromagnetic Dy – O – Fe^T exchange interaction strongly affects the frequency of 411 cm⁻¹ mode below magnetic ordering temperature and is responsible for the noticed anomalous positive frequency shift of this mode.

In order to determine the strength of the spin-phonon coupling of these modes, the influence of the spin-phonon coupling effect on the phonon frequency $\Delta\omega_{s-ph}(T)$ should be separated from the anharmonic contribution $\omega_{anh}(T)$. This is usually done by taking the difference between the measured frequency and the expected anharmonic contribution (see Eq. (1)), $\Delta\omega_{s-ph}(T) = \omega(T) - \omega_{anh}(T)$. The temperature dependence of $|\Delta\omega_{s-ph}|$ for the four phonons modes from Fig. 3 is presented in Fig. 5.

According to the mean-field approximation, and considering an interaction between the nearest-neighbor spins localized at the i th and j th site, the spin–spin correlation function $\langle \mathbf{S}_i \cdot \mathbf{S}_j \rangle$ is proportional to the square of normalized magnetization:

$$\langle \mathbf{S}_i \cdot \mathbf{S}_j \rangle = \left(\frac{M(T)}{M_0} \right)^2, \quad (5)$$

where $M(T)$ is spontaneous magnetization at temperature T and M_0 is the maximal value of spontaneous magnetization [48]. Comparing Eqs. (2) and (5), the frequency shift due to the spin-phonon coupling $\Delta\omega_{s-ph}(T)$ should scale with the $(M(T)/M_0)^2$ curve. The $(M(T)/M_0)^2$ curve was obtained using a numerical solution of the Brillouin function [49] for the case of $S = 5/2$ (for Fe and Dy ions). From Fig. 5 it can be seen that the $|\Delta\omega_{s-ph}|(T)$ for each mode scales very well with $(M(T)/M_0)^2$ curve (solid lines), confirming that the observed significant frequency deviation of these modes from the anharmonic behavior below T_C , originates from the spin-phonon coupling effects.

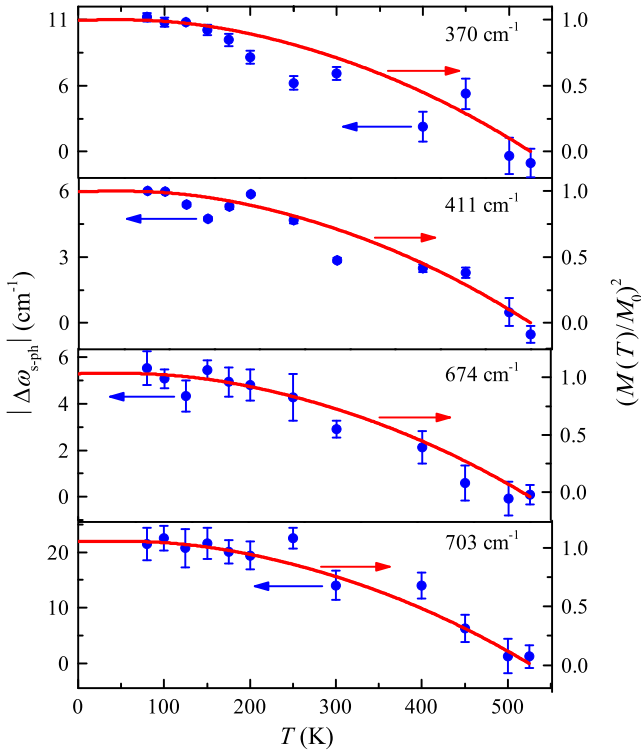


Fig. 5. Temperature dependences of $|\Delta\omega_{s\text{-ph}}|$ (left axis, blue circles) compared with the theoretically obtained curve $(M(T)/M_0)^2$ (right axis, solid lines) for the 370, 411, 674, and 703 cm^{-1} phonon modes.

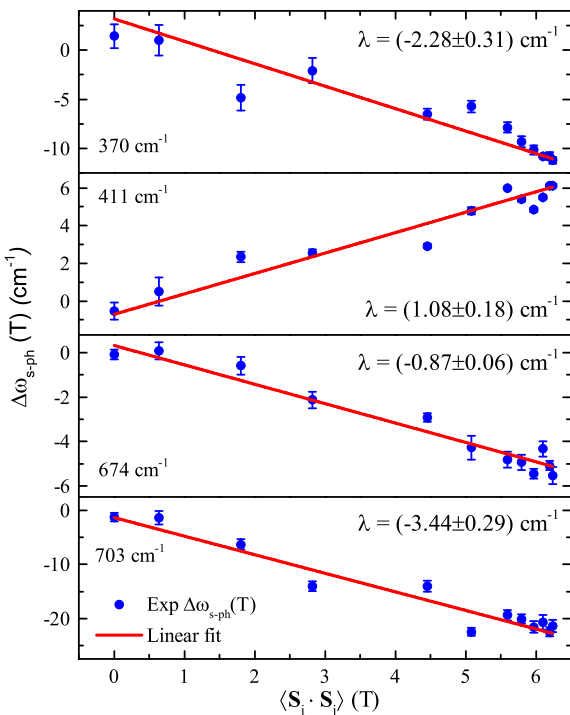


Fig. 6. The plot of $\Delta\omega_{s\text{-ph}}(T)$ vs. $\langle \mathbf{S}_i \cdot \mathbf{S}_j \rangle(T)$ for anomalous phonon modes from Fig. 5 (blue circles). The solid lines are linear fits to the data. The obtained values for spin-phonon coupling constant, λ , are presented for each mode.

According to the Eqs. (2) and (5), the spin-phonon coupling constant λ , as a measure of the strength of the spin-phonon interaction, can be deduced from the plot $\Delta\omega_{s\text{-ph}}(T)$ vs. spin–spin correlation function $\langle \mathbf{S}_i \cdot \mathbf{S}_j \rangle(T)$. The plot of $\Delta\omega_{s\text{-ph}}(T)$ vs. $\langle \mathbf{S}_i \cdot \mathbf{S}_j \rangle(T)$ for four anomalous phonon modes is presented in Fig. 6, where the solid lines represent a linear fit of the data.

The spin-phonon coupling constants λ were determined from the slopes of the linear fits, and λ values are given for each mode in Fig. 6. From this study it can be deduced that λ values obtained by this approach are comparable for all four modes, but have different signs. This result implies that competitive FM and AFM exchange interactions affect the Raman modes differently. The negative values of λ , which are larger for the 703 and 370 cm^{-1} modes than for the 674 cm^{-1} mode, imply that these two modes are more affected by FM ordering. The positive sign for the 411 cm^{-1} mode implies that this mode is dominantly influenced by AFM ordering. Since these modes originate from different vibrations between magnetic ions, it can be concluded that the relative strength of FM or AFM interactions and their contributions to the particular Raman mode are closely related to the vibrational pattern of the mode.

4. Conclusion

We presented the influence of spin-phonon coupling interaction on the phonon modes in nanocrystalline $\text{Dy}_3\text{Fe}_5\text{O}_{12}$ using Raman spectroscopy. The nanocrystalline $\text{Dy}_3\text{Fe}_5\text{O}_{12}$ was prepared by an aqueous sol–gel method synthesis method and the crystal structure, morphology and composition were investigated by XRD, TEM and Raman measurements. From the temperature evolution of the Raman modes, it is shown that four phonon modes from middle- and high-frequency regions displayed significant frequency deviation from the expected anharmonic behavior below T_C . It is concluded that the spin-phonon interaction lies behind the observed anomalous frequency behavior. Different Raman modes exhibited negative or positive shifts with respect to the anharmonicity. Raman modes at 370, 674 and 703 cm^{-1} , which were assigned to the internal tetrahedral (FeO_4) vibrations, experienced negative frequency shift with respect to the anharmonicity due to resultant FM interaction among tetrahedral Fe^{3+} ions. The Raman mode at 411 cm^{-1} , which involves the motion of dodecahedral Dy^{3+} and tetrahedral Fe^{3+} ions, was found to be more sensitive to the AFM exchange interaction between these ions. Within the mean-field approach, the spin–spin correlation function was related to the phonon frequency shift and the spin-phonon coupling strength was estimated for each mode. It was concluded that the coupling of Raman modes with FM or AFM ordering as well as, the strength of this coupling are largely dependent on the vibrational pattern of the particular mode. This study provides a foundation for a better understanding of the fundamental physical properties of $\text{Dy}_3\text{Fe}_5\text{O}_{12}$ based on complex magnetic behavior, thus providing valuable information for the optimization and development of spintronic devices in the near future.

Acknowledgments

The authors acknowledge funding provided by the Institute of Physics Belgrade and the Serbia-India bilateral project through the Grants No: 451-03-47/2023-01/200024 and No: 451-02-697/2022-09/02 of the Ministry of Science, Technological Development and Innovation of the Republic of Serbia. The authors B.R. and N.K. acknowledge the support from the Department of Science and Technology, Govt. of India through India Serbia Joint S and T project (DST/INT/IND-SERBIA/2022/2).

Declaration of competing interests

The authors declare that they have no known competing financial interests or personal relationships that could have appeared to influence the work reported in this paper.

References

- [1] F. Sayetat, Huge magnetostriction in $Tb_3Fe_5O_{12}$, $Dy_3Fe_5O_{12}$, $Ho_3Fe_5O_{12}$, $Er_3Fe_5O_{12}$ garnets, *J. Magn. Magn Mater.* 58 (1986) 334–346.
- [2] W.R. Eppler, M.H. Kryder, Garnets for short wavelength magneto-optic recording, *J. Phys. Chem. Solid.* 56 (1995) 1479–1490.
- [3] T. Yoshimoto, T. Goto, R. Isogai, Y. Nakamura, H. Takagi, C.A. Ross, M. Inoue, Magnetophotonic crystal with cerium substituted yttrium iron garnet and enhanced Faraday rotation angle, *Opt Express* 24 (2016) 8746–8753.
- [4] R. Booth, E. White, Magneto-optic properties of rare earth iron garnet crystals in the wavelength range 1.1–1.7 μ m and their use in device fabrication, *J. Phys. D Appl. Phys.* 17 (2000) 579–587.
- [5] M.H. Phan, M.B. Morales, C.N. Chinnasamy, B. Latha, V.G. Harris, H. Srikanth, Magnetocaloric effect in bulk and nanostructured $Gd_3Fe_5O_{12}$ materials, *J. Phys. D Appl. Phys.* 42 (2009) 115007.
- [6] N. Hur, S. Park, S. Guha, A. Borissov, V. Kiryukhin, S.-W. Cheong, Low-field magnetodielectric effect in terbium iron garnets, *Appl. Phys. Lett.* 87 (4) (2005) 042901.
- [7] S.M. Zanjani, M.C. Onbasli, Thin film rare earth iron garnets with perpendicular magnetic anisotropy for spintronic applications, *AIP Adv.* 9 (2019) 035024.
- [8] C. Suchomski, C. Reitz, D. Pajić, Z. Jagličić, I. Djerdj, T. Brezesinski, Large-pore mesoporous $Ho_3Fe_5O_{12}$ thin films with strong room temperature perpendicular magnetic anisotropy by sol-gel processing, *Chem. Mater.* 26 (2014) 2337–2343.
- [9] W. Wang, R. Chen, X. Qi, Analysis on three-sublattice model of magnetic properties in rare-earth iron garnets under high magnetic fields, *J. Alloys Compd.* 512 (2012) 128–131.
- [10] A. Boutaba, M. Lahoubi, V. Varazashvili, S. Pu, Magnetic, magneto-optical and specific heat studies of the low temperature anomalies in the magnetodielectric Dy_3G ferrite garnet, *J. Magn. Magn Mater.* 476 (2019) 551–558.
- [11] Y. Tokunaga, S. Iguchi, T. Arima, Y. Tokura, Magnetic-field-induced ferroelectric state in $DyFeO_3$, *Phys. Rev. Lett.* 101 (2008) 097205.
- [12] K.M. Song, Y.A. Park, K.D. Lee, B.K. Yun, M.H. Jung, J. Cho, J.H. Jung, N. Hur, Magnetodielectric effect via a noncollinear-to-collinear spin reorientation in rare-earth iron garnets, *Phys. Rev. B* 83 (2011) 012404.
- [13] P.J. von Ranke, B.P. Alho, E.J.R. Plaza, A.M.G. Carvalho, V.S.R. de Sousa, N.A. de Oliveira, Theoretical investigation on the magnetocaloric effect in garnets $R_3Fe_5O_{12}$ where ($R=Y$ and Dy), *J. Appl. Phys.* 106 (2009) 053914.
- [14] C. Li, G.O. Barasa, Y. Qiu, S. Yuan, Magnetocaloric effect and sign reversal of magnetic entropy change across the spin reorientation temperature in $R_3Fe_5O_{12}$ ($R=Gd$, Dy), *J. Alloys Compd.* 820 (2020) 153138.
- [15] J.J. Bauer, E.R. Rosenberg, S. Kundu, K.A. Mkhoyan, P. Quarterman, A.J. Grutter, B.J. Kirby, J.A. Borchers, C.A. Ross, Dysprosium iron garnet thin films with perpendicular magnetic anisotropy on silicon, *Adv. Electron. Mater.* 6 (2020) 1900820.
- [16] M. Deb, P. Molho, B. Barbara, J.-Y. Bigot, Controlling laser-induced magnetization reversal dynamics in a rare-earth iron garnet across the magnetization compensation point, *Phys. Rev. B* 97 (2018) 134419.
- [17] C.Y. Tsai, H.M. Cheng, H.R. Chen, K.F. Huang, L.N. Tsai, Y.H. Chu, C.H. Lai, W.F. Hsieh, Spin and phonon anomalies in epitaxial self-assembled $CoFe_2O_4$ - $BaTiO_3$ multiferroic nanostructures, *Appl. Phys. Lett.* 104 (2014) 252905.
- [18] K.S. Olsson, J. Choe, M. Rodriguez-Vega, G. Khalsa, N.A. Benedek, J. He, B. Fang, J. Zhou, G.A. Fiete, X. Li, Spin-phonon interaction in yttrium iron garnet, *Phys. Rev. B* 104 (2021) L020401.
- [19] J.P. Hurrell, S.P.S. Porto, I.F. Chang, S.S. Mitra, R.P. Bauman, Optical phonons of yttrium aluminum garnet, *Phys. Rev.* 173 (1968) 851–856.
- [20] G. Mace, G. Schaack, T. Ng, J.A. Koningsstein, Optical phonons of terbium-, dysprosium-, and ytterbium-garnet, *Phys. B Condens. Matter* 230 (1970) 391–402.
- [21] J.-J. Song, P.B. Klein, R.L. Wadsack, M. Selders, S. Mroczkowski, R.K. Chang, Raman-active phonons in aluminum, gallium, and iron garnets, *J. Opt. Soc. Am.* 63 (1973) 1135–1140.
- [22] J.-M. Costantini, S. Miro, F. Beuneu, M. Toulemonde, Swift heavy ion-beam induced amorphization and recrystallization of yttrium iron garnet, *J. Phys. Condens. Matter* 27 (2015) 496001.
- [23] P. Grunberg, J.A. Koningsstein, L.G.V. Uitert, Optical phonons in iron garnets, *J. Opt. Soc. Am.* 61 (1971) 1613–1617.
- [24] K. Papagelis, G. Kanellis, S. Ves, G. Kourouklis, Lattice dynamical properties of the rare earth aluminum garnets ($RE_3Al_5O_{12}$), *Phys. Status Solidi B* 233 (2002) 134–150.
- [25] P. Fechine, E. Silva, A. de Menezes, J. Derov, J. Stewart, A. Drehman, I. Vasconcelos, A. Ayala, L. Cardoso, A. Sombra, Synthesis, structure and vibrational properties of $GdIG_x:YIG_{1-x}$ ferrimagnetic ceramic composite, *J. Phys. Chem. Solid.* 70 (2009) 202–209.
- [26] P.G. Klemens, Anharmonic decay of optical phonons, *Phys. Rev.* 148 (1966) 845–848.
- [27] E. Aytan, B. Debnath, F. Kargar, Y. Barlas, M.M. Lacerda, J.X. Li, R.K. Lake, J. Shi, A.A. Balandin, Spin-phonon coupling in antiferromagnetic nickel oxide, *Appl. Phys. Lett.* 111 (2017) 252402.
- [28] D.J. Lockwood, M.G. Cottam, The spin-phonon interaction in FeF_2 and MnF_2 studied by Raman spectroscopy, *J. Appl. Phys.* 64 (1988) 5876–5878.
- [29] E. Granado, A. García, J.A. Sanjurjo, C. Rettori, I. Torriani, F. Prado, R.D. Sánchez, A. Caneiro, S.B. Oseroff, Magnetic ordering effects in the Raman spectra of $La_{1-x}Mn_{1-x}O_3$, *Phys. Rev. B* 60 (1999) 11879–11882.
- [30] D.J. Lockwood, Spin-phonon interaction and mode softening in NiF_2 , *Low Temp. Phys.* 28 (2002) 505–509.
- [31] J. Laverdière, S. Jandl, A.A. Mukhin, V.Y. Ivanov, V.G. Ivanov, M.N. Iliev, Spin-phonon coupling in orthorhombic $RMnO_3$ ($R=Pr, Nd, Sm, Eu, Gd, Tb, Dy, Ho, Y$): A Raman study, *Phys. Rev. B* 73 (2006) 214301.
- [32] C. Kant, J. Deisenhofer, T. Rudolf, F. Mayr, F. Schrettle, A. Loidl, V. Gnezdilov, D. Wulferding, P. Lemmens, V. Tsurkan, Optical phonons, spin correlations, and spin-phonon coupling in the frustrated pyrochlore magnets $CdCr_2O_4$ and $ZnCr_2O_4$, *Phys. Rev. B* 80 (2009) 214417–214426.
- [33] J.A. Moreira, A. Almeida, W.S. Ferreira, J.E. Araújo, A.M. Pereira, M.R. Chaves, J. Kreisel, S.M.F. Vilela, P.B. Tavares, Coupling between phonons and magnetic excitations in orthorhombic $Eu_{1-x}Mn_xO_3$, *Phys. Rev. B* 81 (2010) 054447.
- [34] X.-B. Chen, N.T. Minh Hien, K. Han, J. Chul Sur, N.H. Sung, B.K. Cho, I.-S. Yang, Raman studies of spin-phonon coupling in hexagonal $BaFe_{12}O_{19}$, *J. Appl. Phys.* 114 (2013) 013912.
- [35] P.-H. Shih, C.-L. Cheng, S.Y. Wu, Short-range spin-phonon coupling in in-plane CuO nanowires: a low-temperature Raman investigation, *Nanoscale Res. Lett.* 8 (398) (2013).
- [36] A. Ahlawat, S. Satapathy, S. Maan, V.G. Sathe, P.K. Gupta, Correlation of structure and spin-phonon coupling in (La, Nd) doped $BiFeO_3$ films, *J. Raman Spectrosc.* 45 (2014) 958–962.
- [37] Y. Sharma, S. Sahoo, W. Perez, S. Mukherjee, R. Gupta, A. Garg, R. Chatterjee, R.S. Katiyar, Phonons and magnetic excitation correlations in weak ferromagnetic $YCrO_3$, *J. Appl. Phys.* 115 (2014) 183907.
- [38] C.-S. Chen, C.-S. Tu, P.-Y. Chen, V.H. Schmidt, Z.-R. Xu, Y. Ting, Spin-lattice coupling phase transition and phonon anomalies in bismuth ferrite $BiFeO_3$, *J. Alloys Compd.* 687 (2016) 442–450.
- [39] R.X. Silva, M.C.C. Júnior, S. Yáñez-Vilar, M.S. Andújar, J. Mira, M.A. Señaris-Rodríguez, C.W.A. Paschoal, Spin-phonon coupling in multiferroic Y_2CoMnO_6 , *J. Alloys Compd.* 690 (2017) 909–915.
- [40] W. Baltensperger, J.S. Helman, Influence of magnetic order in insulators on the optical phonon frequency, *Helv. Phys. Acta* 41 (1968) 668–673.
- [41] K. Wakamura, T. Arai, Effect of magnetic ordering on phonon parameters for infrared active modes in ferromagnetic spinel $CdCr_2S_4$, *J. Appl. Phys.* 63 (1988) 5824–5829.
- [42] R. Pauthenet, Spontaneous magnetization of some garnet ferrites and the aluminum substituted garnet ferrites, *J. Appl. Phys.* 29 (1958) 253–255.
- [43] M. Uemura, T. Yamagishi, S. Ebisu, S. Chikazawa, S. Nagata, A double peak of the coercive force near the compensation temperature in the rare earth iron garnets, *Philos. Mag. A* 88 (2008) 209–228.
- [44] T.D. Kang, E.C. Standard, P.D. Rogers, K.H. Ahn, A.A. Sirenko, A. Dubroka, C. Bernhard, S. Park, Y.J. Choi, S.-W. Cheong, Far-infrared spectra of the magnetic exchange resonances and optical phonons and their connection to magnetic and dielectric properties of $Dy_3Fe_5O_{12}$ garnet, *Phys. Rev. B* 86 (2012) 144112.
- [45] D.T.T. Nguyet, N.P. Duong, T. Satoh, L.N. Anh, T.T. Loan, T.D. Hien, Crystallization and magnetic characterizations of dyig and hoig nanopowders fabricated using citrate sol-gel, *J. Sci.: Adv. Mater. Devices* 1 (2016) 193–199.
- [46] R. Nakamoto, B. Xu, C. Xu, H. Xu, L. Bellaïche, Properties of rare-earth iron garnets from first principles, *Phys. Rev. B* 95 (2017) 024434.
- [47] T. Bayaraa, C. Xu, D. Campbell, L. Bellaïche, Tuning magnetization compensation and Curie temperatures in epitaxial rare earth iron garnet films, *Phys. Rev. B* 100 (2019) 214412.
- [48] K. Yosida, Theory of Magnetism, Springer-Verlag Berlin Heidelberg, 1996.
- [49] V. Barsan, V. Kuncser, Exact and approximate analytical solutions of Weiss equation of ferromagnetism and their experimental relevance, *Phil. Mag. Lett.* 97 (2017) 359–371.